

# Local chemical bonding and structural properties in $\text{Ti}_3\text{AlC}_2$ MAX phase and $\text{Ti}_3\text{C}_2\text{T}_x$ MXene probed by Ti 1s x-ray absorption spectroscopy

Martin Magnuson<sup>\*</sup> and Lars-Åke Näslund

Department of Physics, Chemistry and Biology (IFM), Linköping University, SE-581 83 Linköping, Sweden

(Received 30 June 2020; accepted 10 September 2020; published 29 September 2020)

The chemical bonding within the transition-metal carbide materials MAX phase  $\text{Ti}_3\text{AlC}_2$  and MXene  $\text{Ti}_3\text{C}_2\text{T}_x$  is investigated by x-ray absorption near-edge structure (XANES) and extended x-ray absorption fine-structure (EXAFS) spectroscopies. MAX phases are inherently nanolaminated materials that consist of alternating layers of  $M_{n+1}X_n$  and monolayers of an A-element from the IIIA or IVA group in the Periodic Table, where  $M$  is a transition metal and  $X$  is either carbon or nitrogen. Replacing the A-element with surface termination species  $T_x$  will separate the  $M_{n+1}X_n$ -layers forming two-dimensional (2D) flakes of  $M_{n+1}X_nT_x$ . For  $\text{Ti}_3\text{C}_2\text{T}_x$  the  $T_x$  corresponds to fluorine (F) and oxygen (O) covering both sides of every single 2D  $M_{n+1}X_n$ -flake. The Ti  $K$ -edge (1s) XANES of both  $\text{Ti}_3\text{AlC}_2$  and  $\text{Ti}_3\text{C}_2\text{T}_x$  exhibit characteristic preedge absorption regions of C  $2p$ -Ti  $3d$  hybridization with clear crystal-field splitting while the main-edge absorption features originate from the Ti  $1s \rightarrow 4p$  excitation, where only the latter shows sensitivity toward the fcc-site occupation of the termination species. The coordination numbers obtained from EXAFS show that  $\text{Ti}_3\text{AlC}_2$  and  $\text{Ti}_3\text{C}_2\text{T}_x$  are highly anisotropic with a strong in-plane contribution for Ti and with a dynamic out-of-plane contribution from the Al monolayers and termination species, respectively. As shown in the temperature-dependent measurements, the O contribution shifts to shorter bond length while the F diminishes as the temperature is raised from room temperature up to 750 °C.

DOI: [10.1103/PhysRevResearch.2.033516](https://doi.org/10.1103/PhysRevResearch.2.033516)

## I. INTRODUCTION

Despite the large interest in graphene [1], which lacks a natural band gap, it has been difficult to artificially produce graphene-based materials with suitable band gaps. This has encouraged researchers to explore other two-dimensional (2D) materials such as hexagonal boron nitride ( $h$ -BN), molybdenum disulfide ( $\text{MoS}_2$ ), tungsten disulfide ( $\text{WS}_2$ ), and MXenes ( $M_{n+1}X_nT_x$ ). The last example is also the latest 2D material, developed in the past decade, and it consists of a family of 2D transition-metal carbides denoted  $M_{n+1}X_nT_x$  ( $n = 1, 2, 3$ ), where  $M$  is a transition metal,  $X$  is either carbon or nitrogen, and  $T_x$  denotes surface termination species [2–4]. The layered structures contain more than one element, thus they offer properties that may be useful for transistors and spintronics [5], 2D-based electronics and screens [6], in addition to energy storage systems such as supercapacitors [7], Li-ion batteries [8], fuel and solar cells [9], as well as transparent conductive electrodes [10] and composite materials with high strength [11].

The parent precursor compounds of MXenes are inherently nanolaminated materials known as MAX phases

( $M_{n+1}AX_n$ ,  $n = 1, 2, 3$ ) [12] (space group  $P6_3/mmc$ ), where  $A$  is a  $p$ -element that usually belongs to groups IIIA or IVA in the Periodic Table. These phases contain more than 150 variants [13], including  $\text{Ti}_3\text{AlC}_2$ , which is a precursor for the  $\text{Ti}_3\text{C}_2\text{T}_x$  MXene. To make MXene from  $M_{n+1}AX_n$ , the weakly bound A-layers are etched away and replaced by surface termination groups ( $T_x$ ) in the exfoliation process [2]. The delamination results in weakly bound stacks of 2D sheets with  $M_{n+1}X_nT_x$  composition.

Generally, MXenes consist of a core of a few atoms thick 2D  $M_{n+1}X_n$  conductive carbide layer that is crystalline in the basal plane and a transition-metal surface that can be functionalized for different material properties by changing the chemistry of the termination species. Layered structures like MXenes contain more than one element and can therefore offer better variations of physical properties than pure materials, such as graphene, since they can provide a larger number of compositional variables that can be tuned for specific properties. Figure 1 shows schematic side views of the  $\text{Ti}_3\text{AlC}_2$ ,  $\text{Ti}_3\text{C}_2\text{T}_x$ , and TiC structures where the blue and black spheres are the Ti and C atoms, respectively, with strong covalent bonds in the conductive carbide core layer. The stacking of the Ti and C atoms forms three monolayers of Ti and two monolayers of C in an alternated sequence. In  $\text{Ti}_3\text{AlC}_2$  the  $\text{Ti}_3\text{C}_2$  layers are alternated with monolayers of Al, highlighted in Fig. 1 as yellow spheres, while  $\text{Ti}_3\text{C}_2\text{T}_x$  shows purple and red spheres on both sides of the transition-metal carbide that are the F and O atoms, respectively, terminating the surfaces. Two alternatives for the F and O atoms to coordinate on the  $\text{Ti}_3\text{C}_2$  surfaces are the *threefold hollow face-centered-cubic* (fcc) sites and the *threefold hollow hexagonal-close-packed*

\*Corresponding author: [Martin.Magnuson@liu.se](mailto:Martin.Magnuson@liu.se)

Published by the American Physical Society under the terms of the [Creative Commons Attribution 4.0 International](https://creativecommons.org/licenses/by/4.0/) license. Further distribution of this work must maintain attribution to the author(s) and the published article's title, journal citation, and DOI. Funded by [Bibsam](https://www.bibsam.se/).

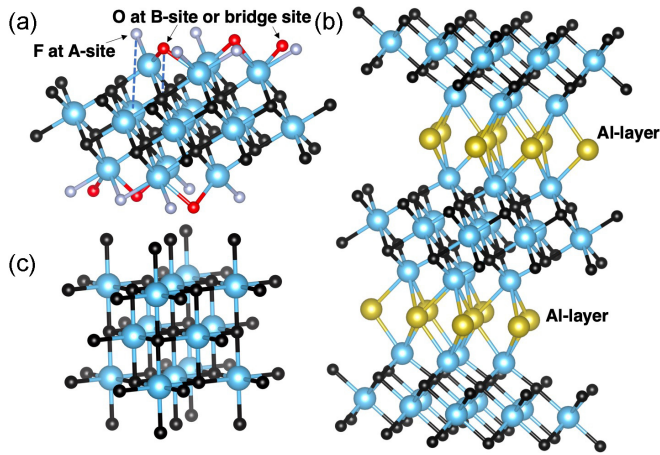


FIG. 1. Structure of an  $M_3C_2T_x$  MXene layer with various termination sites of  $-T_x$ :  $-F$  (purple) and  $-O$  (red). The F atoms are adsorbed in a *threefold hollow fcc site* (A-site). In this model structure the O atoms are in a bridge site between two Ti and in a three-fold hollow hcp site (B-site). Blue and black spheres are Ti and C atoms, respectively, with strong covalent bonds in the  $M_3X_2$  conductive carbide core layer.

(hcp) sites [14–17]; an fcc site is formed by three surface Ti atoms in a triangular formation where the center of the triangle is above a Ti atom in the second (middle) Ti monolayer, while an hcp site is formed by three surface Ti atoms in a triangular formation where the center of the triangle is above a C atom in the adjacent C monolayer. Other alternative coordination sites are on top of the surface Ti atoms or in *bridge sites* between two Ti atoms [14]. The fcc site (also called *A-site*) as the preferred site for the termination species on  $Ti_3C_2T_x$  has been confirmed experimentally using high-resolution transmission electron microscopy (HRTEM) and x-ray photoelectron spectroscopy (XPS) [18]. The combined HRTEM/XPS study found that F only occupies the fcc sites in competition with O and that O also occupies other sites, e.g., bridge sites or on-top sites, but not the hcp sites (also called *B sites*). The study found no terminating species other than F and O and that F desorbs at elevated temperatures ( $>550^\circ\text{C}$ ).

Despite vast interest in MXenes in general, and in  $Ti_3C_2T_x$  in particular, there is little known experimentally about the bonding between the transition metals and the terminating species,  $T_x$ . Previous work of MXenes’ electronic structure has mainly been based on ground-state density functional theory (DFT) calculations at 0 K [14–17,19]. Many of the theoretical investigations find no obstacles regarding replacing the inherently formed termination species with others in the pursuit of tailoring the properties for specific applications. Yet there is no indisputably experimental evidence showing that the inherently formed termination species can be replaced (retermination) [20]. The different theoretical and experimental results and experiences show how important it is to fully understand the bonding conditions at the surfaces of the MXenes.

In this work, we will elucidate the local structural properties and interactions around the Ti atoms in  $Ti_3AlC_2$  and  $Ti_3C_2T_x$  through synchrotron radiation-based Ti *K*-edge ( $1s$ ) x-ray absorption spectroscopy, including both x-ray absorp-

tion near-edge structure (XANES) and extended x-ray absorption fine structure (EXAFS). XANES probes the unoccupied density of states of the absorbing atoms and is therefore an ideal technique for determining the chemical surroundings and local bonding structure around the transition metal. The  $1s$  electron transition can, as a consequence of the selection rule, only occur to molecular orbitals with *p*-character (electric dipole transition) and *d*-character (electric quadrupole transition), although the probability of the  $1s \rightarrow 3d$  transitions is about one-thousandth that of the  $1s \rightarrow np$  transitions [21,22]. EXAFS provides information about the coordination numbers, atomic distances, and amount of atomic displacements and disorder around the probed element [23].

Ti  $1s$  XANES and EXAFS spectra of  $Ti_3AlC_2$  and  $Ti_3C_2T_x$  have been presented previously [24–26]. Yet a detailed analysis of the spectra remains to be performed. Instead of only comparing the Ti  $1s$  XANES and EXAFS spectra of different compounds for similarities (or not) or a crude estimate of the Ti oxidation state, as in previous XANES and/or EXAFS studies of MAX-phases and MXenes [24–30], our aim in the present work is to learn more about the local bonding around the probed Ti atoms in both  $Ti_3AlC_2$  and  $Ti_3C_2T_x$  through distinguished Ti  $1s$  XAS features.

The  $Ti_3C_2T_x$  samples were fabricated as freestanding foils through wet etching, which leads to inherent F and O terminations [18]. Through heat treatments, the fcc site coordinated F will desorb and be replaced by O, which prefers the fcc site when it is available [18]. The change of the fcc coordination will induce modifications in the XANES and EXAFS spectra, thus it will reveal local information on the bonding situation between the transition-metal atoms and termination species. Hence, the study demonstrates how x-ray absorption spectroscopy can be used to probe the MXene surfaces to shed more light on the local chemical interaction between F, O, and Ti atoms, which is relevant knowledge when designing MXenes for sought-after material properties.

## II. EXPERIMENTAL DETAILS

### A. Sample preparation

Powders of  $Ti_3AlC_2$  were produced starting with a mixture of TiC (Alfa Aesar, 98+%), Ti (Alfa Aesar, 98+%), and Al (Alfa Aesar, 98+%) in 1:1:2 molar ratios. The mixture was processed in a mortar with a pestle for 5 min and thereafter inserted in an alumina tube furnace. With a continuous stream of Ar gas, the furnace was heated at a rate of  $5^\circ\text{C min}^{-1}$  up to  $1450^\circ\text{C}$  and held for 280 min before cooling down to room temperature. The resulting material is a lightly sintered  $Ti_3AlC_2$  sample, which is then crushed to a powder with particle size  $< 60 \mu\text{m}$  using a mortar and pestle. A few mg of the  $Ti_3AlC_2$  powder was mixed with polyethylene powder (Aldrich, 40–48  $\mu\text{m}$  particle size) and thereafter cold-pressed into an  $\sim 500\text{-}\mu\text{m}$ -thick pellet for the x-ray absorption spectroscopy.

To convert the  $Ti_3AlC_2$  to  $Ti_3C_2T_x$  flakes, half a gram of  $Ti_3AlC_2$  powder was added to a premixed 10 mL aqueous solution of 12 M HCl (Fisher, technical grade) and 2.3 M LiF (Alfa Aesar, 98+%) in a Teflon bottle. Prior to adding the MAX powder to the HCl/LiF(aq) solution, the latter was

placed in an ice bath to avoid the initial overheating that otherwise can be a consequence of the exothermic reaction when the MAX power is added. After 0.5 h in the ice bath, the bottle was placed on a magnetic stirrer hot plate in an oil bath and held at 35 °C for 24 h. The mixture was thereafter washed, first through three cycles using 40 mL of 1 M HCl(aq) and thereafter three cycles using 40 mL of 1 M LiCl (Alfa Aesar, 98+%). Then, the mixture was washed through cycles of 40 mL of deionized water until the supernatant reached a pH of approximately 6. In the end, 45 mL of deionized water was added, which was de-aerated by bubbling N<sub>2</sub> gas through it and sonicated using an ultrasonic bath for 1 h. The resulting suspension was centrifuged for 1 h at 3500 rpm, which removed larger particles. The supernatant produced had a Ti<sub>3</sub>C<sub>2</sub>T<sub>x</sub> concentration of 1 mg mL<sup>-1</sup>. To make freestanding films, 20 mL of the suspension was filtered through a nanopolypropylene membrane (3501 Coated PP, 0.064 μm pore size, Celgard, USA). The obtained Ti<sub>3</sub>C<sub>2</sub>T<sub>x</sub> foil is described in detail in Ref. [7].

Moreover, to observe XANES and EXAFS features originating from termination species, the surfaces must be free from oxidized material, mainly TiO<sub>2</sub> [31]. The newly made Ti<sub>3</sub>C<sub>2</sub>T<sub>x</sub> foils were therefore stored in an argon (Ar) atmosphere and mounted on the sample holder in a glove-bag filled with nitrogen gas (N<sub>2</sub>). A continuous flow of N<sub>2</sub> protected the sample from oxidation during measurement. Hence, the obtained XANES and EXAFS spectra of the Ti<sub>3</sub>C<sub>2</sub>T<sub>x</sub> foils have no detectable contribution from TiO<sub>2</sub> impurities. The insignificant amount of TiO<sub>2</sub> impurities and carbon-containing contamination in the Ti<sub>3</sub>C<sub>2</sub>T<sub>x</sub> samples was confirmed through XPS. The XPS further showed a small amount of adsorbed Cl that desorbed completely at a moderate heat treatment. In addition, no indication of OH termination was observed, which agrees with the combined HRTEM/XPS study [18]. The Ti<sub>3</sub>AlC<sub>2</sub> (and TiC), on the other hand, showed small amounts of TiO<sub>2</sub> impurities in the XPS spectra. Contribution from TiO<sub>2</sub> impurities in the Ti 1s XANES and EXAFS spectra of the Ti<sub>3</sub>AlC<sub>2</sub> (and TiC), therefore, cannot be excluded. Nevertheless, the TiO<sub>2</sub> contribution was shown to be at a negligible level.

### B. XANES and EXAFS analysis

The XANES and EXAFS spectra were measured at the Ti 1s edge using an Si111 crystal in the monochromator at the wiggler beamline BALDER on the 3 GeV electron storage ring at MAX IV in Lund, Sweden. The x-ray absorption of the Ti<sub>3</sub>C<sub>2</sub>T<sub>x</sub> MXene, the Ti<sub>3</sub>AlC<sub>2</sub> MAX phase, a TiC reference, and a Ti metal reference foil were monitored in transmission mode with ionization chambers (*I*<sub>0</sub> : 200 mbar N<sub>2</sub> and He; *I*<sub>1</sub> : 2 bar N<sub>2</sub>). The Ti<sub>3</sub>C<sub>2</sub>T<sub>x</sub> sample was positioned in a water-cooled gas cell (Linkam Scientific Instruments) with a low N<sub>2</sub> flow and a heating element that enabled measurements at different temperatures. The Ti 1s XANES spectra were obtained at room temperature (RT) and at 250 °C after 20 min heat treatments at 250, 550, and 750 °C. The energy resolution at the Ti 1s edge of the beamline monochromator was ~1.0 eV with 0.1 eV energy steps for XANES and 0.2 eV steps for EXAFS. The photon energy scale was calibrated using the first derivative of a Ti foil absorption spectrum, where the

first inflection point was set to 4.9660 keV. The obtained spectra were normalized below the absorption edge before the background intensity subtraction and thereafter normalized above the absorption edge in the photon energy region of 5.045–5.145 keV. Self-absorption effects were found to be negligible in the normal incidence geometry for the Ti<sub>3</sub>C<sub>2</sub>T<sub>x</sub> and the Ti foils. The spectra of the Ti<sub>3</sub>AlC<sub>2</sub> and TiC pellets showed, on the other hand, some self-absorption effects even at normal incidence, and they have therefore been corrected using the simple function  $AI(\epsilon)[1 - BI(\epsilon)]^{-1}$ , where *A* is a scaling factor, *B* is the self-absorption compensation factor, and *I*( $\epsilon$ ) is the Ti 1s XANES spectrum of Ti<sub>3</sub>AlC<sub>2</sub> and TiC, respectively. *A* and *B* are adjusted until the absorption features in the photon energy region of 5.045–5.145 keV have a similar appearance to the Ti 1s XANES spectrum of Ti<sub>3</sub>C<sub>2</sub>T<sub>x</sub>.

The Ti-Ti, Ti-C, Ti-O, and Ti-F scattering paths obtained from the effective scattering amplitudes (FEFF) [32–34] were included in the EXAFS fitting using the Visual Processing in EXAFS Researches (VIPER) software package [35]. The *k*<sup>2</sup>-weighted  $\chi$  EXAFS oscillations were extracted from the raw absorption data, the average of 10 absorption spectra, after removing known monochromator-induced glitches and subsequent atomic background subtraction and normalization. The atomic distances (*R*), number of neighbors (*N*), Debye-Waller factors ( $\sigma^2$ , representing the amount of disorder), and the reduced  $\chi_r^2$  as the squared area of the residual, were determined by fitting the back-Fourier-transform signal between *k* = 0 and 12.5 Å<sup>-1</sup> originally obtained from the forward Fourier transform within *R* = 0–3.35 Å of the first coordination shell using a Hanning window function [32–34] with a many-body factor of  $S_0^2 = 0.8$ . The disorder and high-frequency thermal vibration of the atoms depending on the temperature was accounted for by an increasing Debye-Waller term  $\sigma^2 = \sigma_{\text{stat}}^2 + \sigma_{\text{vib}}^2$  consisting of a static and a vibrational part that was proportional to the difference of the mean-square atomic displacements [36–38].

### III. RESULTS AND DISCUSSION

Figure 2 shows the obtained high-resolution Ti 1s XANES spectra of Ti-metal, TiC, Ti<sub>3</sub>AlC<sub>2</sub>, and Ti<sub>3</sub>C<sub>2</sub>T<sub>x</sub>. The absorption spectra consist of two regions: preedge and main edge. Features in the preedge region of *K*-edge XANES spectra of 3*d* transition-metal compounds are assigned to electric dipole (*1s* → *np*) and quadrupole (*1s* → *3d*) transitions. However, the intensity contribution of the latter is minor because of orbital symmetry restrictions [21,22,39], and preedge features are therefore in most cases assigned to *1s* electron excitation into *p-d* hybridized orbitals, i.e., the transition into the *p*-component of the molecular orbitals that have both *p*- and *d*-character. The intensity of the preedge features depends mainly on coordination, symmetry, and bond angles [40].

The preedge features in the spectrum of the Ti metal reference, peaks *A* and *B* at 4.967 and 4.971 keV, respectively, are typical examples of *1s* → *p-d* hybridized molecular orbital excitation near the Fermi energy (*E*<sub>*f*</sub>) [41]. The sharp peak *A* near the Fermi energy originates from Ti 1s excitation into a local Ti 3*d*-4*p* mixing orbital (internal orbital mixing in the probed element), while peak *B* originates from Ti 1s excitation into hybridized 3*d*-4*p* orbital where the 3*d* contribution

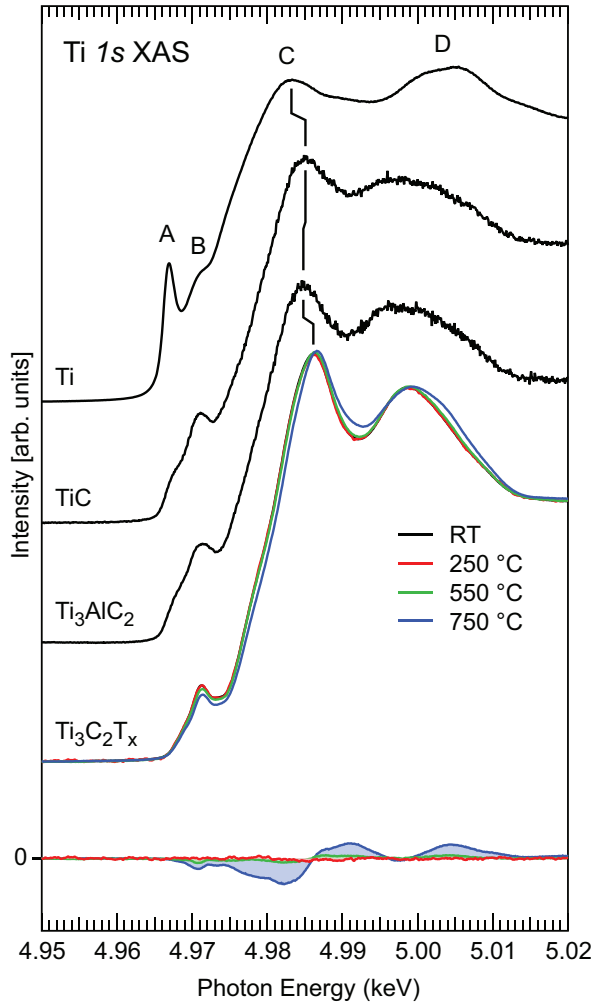


FIG. 2. Ti 1s XANES spectra of Ti metal foil, TiC,  $\text{Ti}_3\text{AlC}_2$ , and  $\text{Ti}_3\text{C}_2\text{T}_x$ . The  $\text{Ti}_3\text{C}_2\text{T}_x$  spectra are recorded at RT and at 250 °C after 20 min heat treatments at 250, 550, and 750 °C. Note that the red spectrum of  $\text{Ti}_3\text{C}_2\text{T}_x$  heat-treated at 250 °C covers the black spectrum of nonheated  $\text{Ti}_3\text{C}_2\text{T}_x$ . The difference of the RT  $\text{Ti}_3\text{C}_2\text{T}_x$  spectrum and the spectra obtained after 250, 550, and 750 °C heat treatment are shown at the bottom.

originates from neighboring Ti atoms [42,43]. The intensity of the preedge features is, however, reduced because of the sixfold coordination of the Ti atoms in the metal [41]. The main-edge region consists of two broad features C (white line) and D that correspond to  $1s \rightarrow 4p$  excitations [43]. With the Ti 1s XANES spectrum of the Ti metal reference, it is possible to estimate the  $E_f$  position, which is located close to the onset of peak A at 4.9642 keV. The full width at half-maximum of peak A of the Ti metal reference (1.3 eV) is also an indication of the good resolution at the Balder beamline.

The XANES spectra of TiC,  $\text{Ti}_3\text{AlC}_2$ , and  $\text{Ti}_3\text{C}_2\text{T}_x$  display significantly different structures compared with the Ti metal reference spectrum (see Fig. 2). The preedge region consists of two features, which are highlighted in Fig. 3. The TiC and  $\text{Ti}_3\text{AlC}_2$  spectra show a shoulder at 4.9679 keV and a peak at 4.9710 and 4.9709 keV, respectively, while the  $\text{Ti}_3\text{C}_2\text{T}_x$  spectrum shows a shoulder at 4.9689 keV and

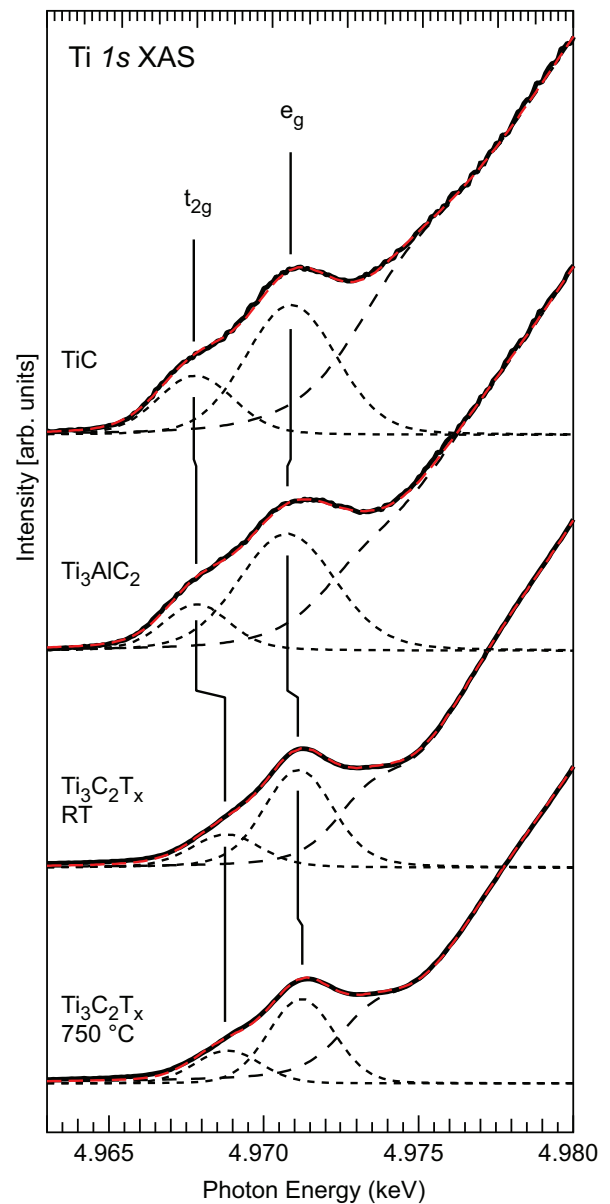


FIG. 3. Curve fitting of the Ti 1s XANES preedge region for TiC,  $\text{Ti}_3\text{AlC}_2$ , room-temperature (RT)  $\text{Ti}_3\text{C}_2\text{T}_x$ , and  $\text{Ti}_3\text{C}_2\text{T}_x$  after 750 °C heat treatment. The dotted lines represent the Ti 1s excitations into the  $t_{2g}$  and  $e_g$  orbitals, and the dashed lines represent the Ti  $1s \rightarrow 4p$  excitations (black) and the accumulated intensity from all Ti 1s excitations (red).

a peak at 4.9711 keV. A basic density-of-states calculation obtained from a simple  $\text{Ti}_3\text{C}_2\text{T}_x$  model with  $\text{T}_x$  being F on the fcc sites and O on the bridge sites shows two C  $2p$  peaks located at 4.2 and 7.1 eV above the  $E_f$  and two Ti  $3d$  peaks located at 4.0 and 6.9 eV above  $E_f$ . The orbital mixing provides the C  $2p$ -Ti  $3d$  hybridization and would correspond to  $\sim 4.968$  and  $\sim 4.971$  keV, respectively, in the Ti 1s XANES, which is close to the two preedge features obtained in the experimental spectra. Hence, the Ti 1s XANES preedge features of TiC,  $\text{Ti}_3\text{AlC}_2$ , and  $\text{Ti}_3\text{C}_2\text{T}_x$  are assigned to Ti  $1s \rightarrow \text{C } 2p - \text{Ti } 3d$  hybridized molecular orbital excitation. The  $\text{Ti}_3\text{C}_2\text{T}_x$  spectrum shows lower intensity in the preedge

region compared to TiC and  $\text{Ti}_3\text{AlC}_2$ , which suggests that the Ti  $1s \rightarrow \text{C } 2p - \text{Ti } 3d$  hybridized molecular orbital excitation is reduced for  $\text{Ti}_3\text{C}_2\text{T}_x$  compared with both TiC and  $\text{Ti}_3\text{AlC}_2$ . The energy difference between the two C  $2p$ -Ti  $3d$  peaks corresponds to the crystal-field splitting of the Ti  $3d$  states into the  $t_{2g}$  and  $e_g$  orbitals [43], thus it can be determined experimentally to be 3.1, 2.9, and 2.2 eV for TiC,  $\text{Ti}_3\text{AlC}_2$ , and  $\text{Ti}_3\text{C}_2\text{T}_x$ , respectively. The absence of a sharp peak near the  $E_f$  in the Ti  $1s$  XANES of TiC,  $\text{Ti}_3\text{AlC}_2$ , and  $\text{Ti}_3\text{C}_2\text{T}_x$  indicates that there is no local unoccupied Ti  $3d$ - $4p$  hybridized orbital available for electron excitation.

The main-edge region shows two peaks, *C* and *D* in Fig. 2, which because of the 2D nature are relatively sharp for  $\text{Ti}_3\text{C}_2\text{T}_x$ . The peaks originate from Ti  $1s \rightarrow 4p$  excitations [43]. In addition, a closer look at the rising edge, i.e., the steep increase in intensity at the main edge, reveals a shoulder at 4.9780 keV. The shoulder is more noticeable in the  $\text{Ti}_3\text{C}_2\text{T}_x$  spectrum, which is because of the high-energy shift of the first main-edge peak *C*; the peak *C* is at 4.9850 and 4.9847 keV for the TiC and  $\text{Ti}_3\text{AlC}_2$  spectra, respectively, while the  $\text{Ti}_3\text{C}_2\text{T}_x$  spectrum has the peak *C* at 4.9861 keV. The position of peak *C* for the TiC and  $\text{Ti}_3\text{AlC}_2$  spectra is almost the same, which suggests that the interaction between the Al layers and the  $\text{Ti}_3\text{C}_2$  layers in  $\text{Ti}_3\text{AlC}_2$  is very weak. The 1.4 eV shift of the *C* peaks between the  $\text{Ti}_3\text{AlC}_2$  and  $\text{Ti}_3\text{C}_2\text{T}_x$  spectra is a consequence of the replacement of the weak interacting Al layers with the stronger interacting termination species  $\text{T}_x$ , where the F and O atoms attract charge from the Ti atoms.

In Fig. 2 there are also Ti  $1s$  XANES spectra of the  $\text{Ti}_3\text{C}_2\text{T}_x$  sample after it has been heated to 250, 550, and 750 °C, respectively. After each heat treatment (to 550 and 750 °C), the sample was brought back to 250 °C before XANES-spectrum recording. As expected, there are no significant changes in the spectra after the heat treatments to 250 and 550 °C, because temperatures above 550 °C are needed to alter the termination of the  $\text{Ti}_3\text{C}_2\text{T}_x$  surfaces [18]. Included in Fig. 2 are also difference spectra that highlight the influence from the heat treatments of the  $\text{Ti}_3\text{C}_2\text{T}_x$  sample. The small deviations from the zero line are inconsiderable for the temperatures 250 and 550 °C, although there is an indication that 550 °C is the temperature threshold onset at which to introduce changes in the  $\text{T}_x$  coordination, which are then reflected in the Ti  $1s$  XANES spectra. A heat treatment to 750 °C (and subsequent cooling to 250 °C) provides, on the other hand, a high-energy shift of the peaks in the main-edge region of 0.5 eV, which has the effect that the preedge region appears to show a slightly reduced intensity. The difference spectrum for the 750 °C spectrum shows the characteristic variations common for a main-edge energy shift and not an intensity redistribution. It is interesting to note that the energy positions of the features in the preedge region are almost not affected by the heat treatment; see Fig. 3. The  $t_{2g}$  peak has the same position while the  $e_g$  peak has shifted 0.1 eV, thus widening the crystal-field splitting slightly. The fact that the preedge region, which mainly originates from Ti  $1s$  excitations into the C  $2p$ -Ti  $3d$  hybridized molecular orbitals in the  $\text{Ti}_3\text{C}_2$  layer, is almost unaffected by the heat treatments is supported by the previous combined HRTEM/XPS study, which found that while removing F from a  $\text{Ti}_3\text{C}_2\text{T}_x$  sample through a heat treatment, the C  $1s$  XPS carbide peak remained unaffected

[18]. The fact that the crystal-field splitting widens to some extent suggests a stronger interaction between the O and the fcc-site compared to F. The main-edge features that originate from the Ti  $1s \rightarrow 4p$  excitation show, on the other hand, a higher sensitivity toward the fcc-site occupation.

The XANES spectra of  $\text{Ti}_3\text{C}_2\text{T}_x$  show some similarities to the XANES spectrum of  $\text{TiO}_2$  [24–27,41,43,44]. A direct comparison shows that the preedge region of  $\text{Ti}_3\text{C}_2\text{T}_x$  has more intensity and a smaller crystal-field splitting. The absorption rising edge of the  $\text{Ti}_3\text{C}_2\text{T}_x$  spectrum is shifted about –3 eV while the absorption energy shift at peak *C* is about –1 eV. A larger difference between the  $\text{Ti}_3\text{C}_2\text{T}_x$  and the  $\text{TiO}_2$  XANES spectra is the shape of peak *D* where the  $\text{TiO}_2$  shows strong peak intensity at 5.0035 keV that is absent in the  $\text{Ti}_3\text{C}_2\text{T}_x$  spectrum before the heat treatment, hence there is no detectable contribution from  $\text{TiO}_2$  impurities in the  $\text{Ti}_3\text{C}_2\text{T}_x$  sample. The Ti  $1s$  XANES spectra of the 750 °C heat treated  $\text{Ti}_3\text{C}_2\text{T}_x$  show a trend of changes—slightly larger crystal-field splitting, 0.5 eV shift of the rising edge and the *C* peak, and the intensity shift in the *D* peak inducing a shoulder at 5.0035 keV—that suggest a stronger Ti-O interaction in heat treated  $\text{Ti}_3\text{C}_2\text{T}_x$  compared to the nontreated  $\text{Ti}_3\text{C}_2\text{T}_x$ . Hence, the Ti  $1s$  XANES supports the observation [18] that F occupies only the fcc sites and that a heat treatment up to 750 °C removes F and makes the fcc sites available for O where the Ti-O interaction becomes stronger. (Experiments with and without the low  $\text{N}_2$  flow in the Linkam gas cell ensured that no oxidation of the  $\text{Ti}_3\text{C}_2\text{T}_x$  sample occurred in the presented work.)

Figure 4 shows the EXAFS structure factor oscillations of  $\text{Ti}_3\text{AlC}_2$  and  $\text{Ti}_3\text{C}_2\text{T}_x$  in comparison with the Ti metal reference, obtained from raw data that have not been phase-shifted. The structure factors  $\chi$ , which are displayed as a function of the wave vector  $k$ , were  $k^2$ -weighted to highlight the higher  $k$ -region, where  $k = \hbar^{-1} \sqrt{2m(E-E_o)}$  is the wave vector of the excited electron in the x-ray absorption process. The frequency of the oscillations and the intensity of the EXAFS signal are directly related to the atomic distance ( $R$ ) and the number of nearest neighbors ( $N$ ), respectively; a higher frequency of the oscillations implies extended  $R$  while an enlarged amplitude implies increased  $N$ .

Starting with Ti metal at the top of Fig. 4, we observe the main oscillations at 4.18, 5.55, and 6.80  $\text{\AA}^{-1}$  where the middle one is caused by the Ti-Ti in-plane scattering that corresponds to the distance for the  $a$ -axis in the hexagonal crystal structure. For  $k$ -values above 12  $\text{\AA}^{-1}$ , the oscillations are damped out and simultaneously the noise increases.

For  $\text{Ti}_3\text{AlC}_2$  and  $\text{Ti}_3\text{C}_2\text{T}_x$ , shown in the middle and bottom of Fig. 4, the main sharp oscillations occur in the 3.4–7.0  $\text{\AA}^{-1}$ - $k$ -space region. There are also peaks at  $k = 4.63$  and 5.83  $\text{\AA}^{-1}$ , i.e., between the main Ti-Ti peaks, that only appear as weak shoulders in the Ti metal. The positions of the three main Ti-Ti peaks in  $\text{Ti}_3\text{AlC}_2$  and  $\text{Ti}_3\text{C}_2\text{T}_x$  (3.93, 5.28, and 6.50  $\text{\AA}^{-1}$ ) are shifted –0.25 to –0.30  $\text{\AA}^{-1}$  in comparison to Ti metal (4.18, 5.55, and 6.80  $\text{\AA}^{-1}$ ) and similar for TiC [45,46]. The small features at low- $k$  values at 1.58 and 2.4–2.7  $\text{\AA}^{-1}$  for the  $\text{Ti}_3\text{C}_2\text{T}_x$  are associated with superimposed oscillations from Ti-O/F scattering.

While the heat treatments do not cause any  $k$ -shifts, the intensities of the oscillations decrease with increasing temperature, except for the oscillation at  $k = 4.63 \text{\AA}^{-1}$ . The

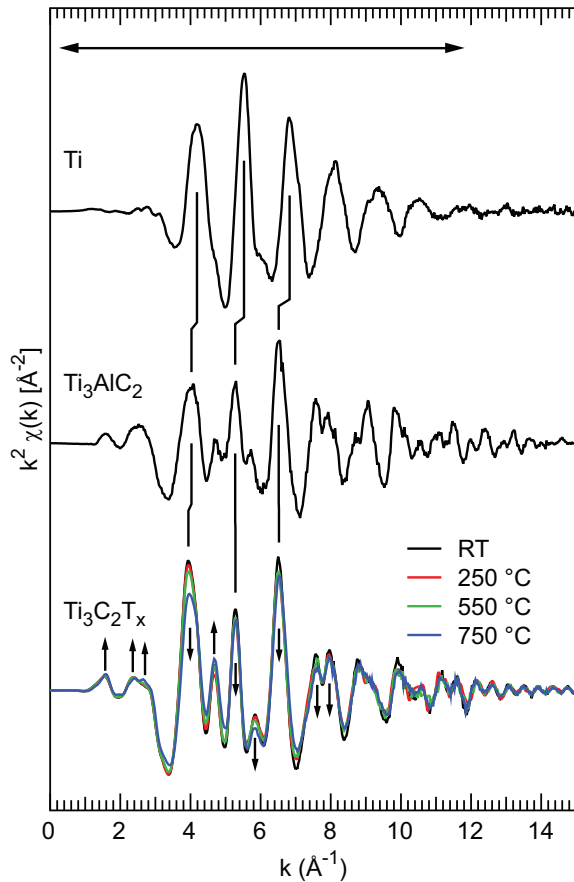


FIG. 4.  $k^2$ -weighted EXAFS,  $k^2\chi(k)$ , as a function of the photoelectron wave number  $k$  of the Ti metal foil,  $\text{Ti}_3\text{AlC}_2$ , and  $\text{Ti}_3\text{C}_2\text{T}_x$  sample. The  $\text{Ti}_3\text{C}_2\text{T}_x$  samples are recorded at RT and at 250 °C after 20 min heat treatments at 250, 550, and 750 °C. The horizontal arrow at the top shows the  $k$ -window for the most pronounced oscillations, and the vertical arrows indicate changes in the peak intensities.

oscillation intensity of the double peak at 7.55–7.95  $\text{\AA}^{-1}$  also decreases with increasing temperature. More interestingly, the small features at 1.58 and 2.4–2.7  $\text{\AA}^{-1}$  are also affected by the heat treatment. To analyze the detailed local structure and atomic distances in the films, Fourier transforms of the EXAFS data were performed.

Figure 5 shows the magnitude of the Fourier transform obtained from the  $k^2$ -weighted EXAFS oscillations  $\chi(k)$  in Fig. 4 by the standard EXAFS procedure [34] related to the radial distribution function. The horizontal arrow at the top of Fig. 4 indicates the applied  $k$ -window. Table I shows the final results of the EXAFS fitting using the FEFF scattering paths of  $\text{Ti}_3\text{AlC}_2$  and  $\text{Ti}_3\text{C}_2\text{T}_x$  and hcp Ti metal as structure model systems. The obtained radius values are in comparison to atomic distances determined for lattice parameters from x-ray diffraction (XRD) in the literature, listed in parentheses in Table I. The initial crystal structure in the modelling assumes a  $\text{Ti}_3\text{C}_2\text{F}_1\text{O}_2$  composition in line with previous quantitative core-level XPS results [18]. However, the obtained atomic distances have sources of errors such as photon energy calibration and dispersion, statistical noise, and inaccuracies in the *ab initio* calculations of scattering paths using FEFF.

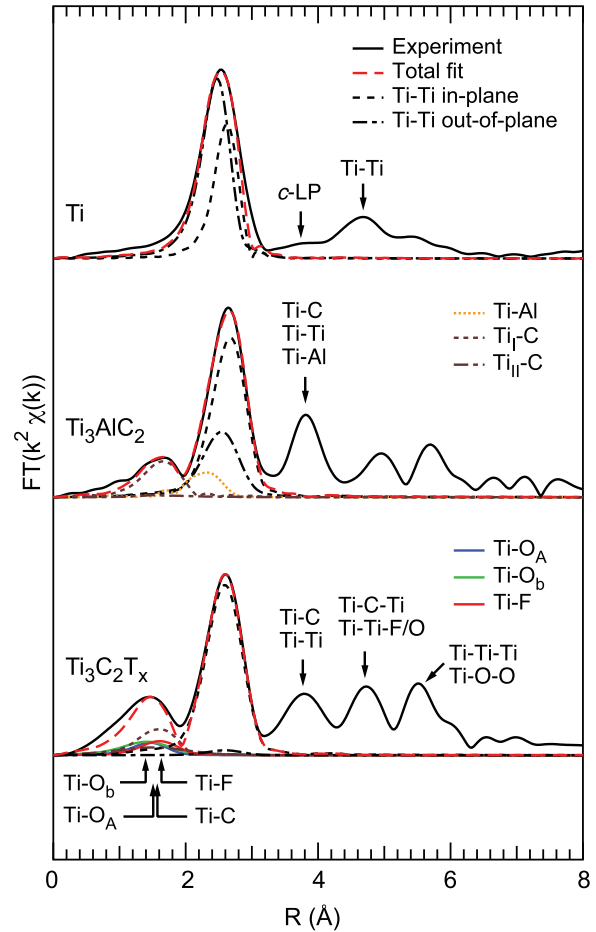


FIG. 5. Fourier transform obtained from the  $k^2$ -weighted EXAFS oscillations  $\chi(k)$  in Fig. 4 of Ti metal foil,  $\text{Ti}_3\text{AlC}_2$ , and  $\text{Ti}_3\text{C}_2\text{T}_x$ .

The corresponding errors in XRD are in the same order of magnitude as for EXAFS.

In Ti metal with hcp structure, the main peak consists of the in-plane Ti-Ti scattering ( $N = 6$ ) at 2.842  $\text{\AA}$  and ( $N = 6$ ) of 2.966  $\text{\AA}$ , where the latter corresponds to the  $a$ -axis of the crystal. For comparison, the peak that consists of the out-of-plane Ti-Ti scattering path of the  $c$ -axis is located at 4.675  $\text{\AA}$  as a weak feature. The corresponding values obtained from XRD measurements are 2.897, 2.950, and 4.686  $\text{\AA}$ , respectively [47]. The more intense peak in Ti metal observed at  $\sim 4.7$   $\text{\AA}$  in Fig. 4 is because of the superposition of the three longer direct Ti-Ti scattering paths with atomic distances 5.079–5.110  $\text{\AA}$  in the higher-order coordination shells.

For  $\text{Ti}_3\text{AlC}_2$ , shown in the middle in Fig. 5, there is a slight shift of the main Ti-Ti peak to larger atomic distance, and a new peak corresponding to Ti-C bonding appears at  $\sim 1.66$   $\text{\AA}$ . In addition, there is a prominent peak at  $\sim 3.8$   $\text{\AA}$  caused by Ti-Ti and Ti-Al scattering from the central Ti layer.

The main peak of the  $\text{Ti}_3\text{C}_2\text{T}_x$ , shown at the bottom in Fig. 5, is dominated ( $N = 4.982$ ) by the in-plane Ti-Ti scattering at 3.016  $\text{\AA}$ ; the in-plane Ti-Ti scattering corresponds to the  $a$ -axis unit-cell edge. The weaker out-of-plane scattering at 3.072  $\text{\AA}$  shows a significantly lower intensity ( $N = 1.312$ ),

TABLE I. Structural parameters for  $\text{Ti}_3\text{AlC}_2$  and  $\text{Ti}_3\text{C}_2\text{T}_x$  in comparison to Ti metal reference obtained from fitting of calculated scattering paths in the first coordination shell.  $N$  is the coordination number,  $R$  is the atomic distance (in Å) for the Ti-Ti and Ti-C scattering paths, respectively,  $\sigma$  is the corresponding Debye-Waller factor representing the amount of atomic displacement and disorder, reduced  $\chi_r^2$  is the squared area of the residual,  $N_{\text{ind}}$  is the number of independent points,  $P$  is the number of fitting parameters, and  $\nu$  is the degrees of freedom. Atomic distances obtained from lattice parameters in XRD are given in parentheses [39].

System	Shell	$R$ (Å) <sup>a</sup>	$N$ <sup>b</sup>	$\sigma$ (Å <sup>2</sup> ) <sup>c</sup>	Statistics
Ti metal (at RT)	6*Ti-Ti	2.842 (2.897)	5.535	0.0042	$\chi_{20}^{0.95} = 8.44$ $N_{\text{ind}} = 28, P = 8$ $\nu = N_{\text{ind}} - P = 20$
	6*Ti-Ti: LP <sup>d</sup> - <i>a</i>	2.966 (2.950)	2.237	0.0014	
	6*Ti-Ti: LP <sup>d</sup> - <i>c</i>	4.675 (4.686)	2.005	0.0077	
$\text{Ti}_3\text{AlC}_2$ (at RT)	3 * Ti <sub>II</sub> -C	2.160 (2.120)	2.764	0.0025	$\chi_4^{0.95} = 9.487$ $N_{\text{ind}} = 24, P = 20$ $\nu = N_{\text{ind}} - P = 4$
	6 * Ti <sub>I</sub> -C	2.220 (2.227)	1.560	0.0025	
	3 * Ti <sub>II</sub> -Al	2.708 (2.781)	1.299	0.0015	
	3*Ti-Ti oop <sup>e</sup>	3.029 (3.069)	1.164	0.0011	
	6*Ti-Ti: LP <sup>d</sup> - <i>a</i>	3.032 (3.075)	5.735	0.0066	
$\text{Ti}_3\text{C}_2\text{T}_x$ (at RT)	1 * Ti <sub>II</sub> -O <sub>A</sub>	1.707	0.199	0.0045	$\chi_{10}^{0.95} = 8.307$ $N_{\text{ind}} = 36, P = 26$ $\nu = N_{\text{ind}} - P = 10$
	1 * Ti <sub>II</sub> -O <sub>B</sub>	1.952	0.292	0.0030	
	1 * Ti <sub>II</sub> -F	2.115	0.245	0.0029	
	6 * Ti <sub>I</sub> -C	2.139	1.992	0.0012	
	3 * Ti <sub>II</sub> -C	2.234	2.057	0.0079	
	6*Ti-Ti: LP <sup>d</sup> - <i>a</i>	3.016 (3.075)	4.982	0.0056	
	3*Ti-Ti oop <sup>e</sup>	3.072 (3.135)	1.312	0.0021	

<sup>a</sup>The errors in the atomic distances are estimated to be  $\pm 0.01$  Å.

<sup>b</sup>The errors in the coordination numbers are estimated to be  $\pm 0.01$ .

<sup>c</sup>The errors in the Debye-Waller factors are estimated to be  $\pm 0.001$  Å<sup>2</sup>.

<sup>d</sup>Lattice parameter.

<sup>e</sup>Out-of-plane.

which is not surprising for a 2D material. As also observed in Fig. 5, the Ti-Ti distances of the in-plane and out-of-plane contributions of  $\text{Ti}_3\text{C}_2\text{T}_x$  (3.016 and 3.072 Å) are located at slightly different distances compared to the Ti-Ti atomic distances in  $\text{Ti}_3\text{AlC}_2$  (3.029 and 3.032 Å). The value of 3.016 Å for the in-plane Ti-Ti distance of  $\text{Ti}_3\text{C}_2\text{T}_x$  is somewhat smaller than the calculated in-plane Ti-Ti atomic distance obtained from the XRD lattice parameter ( $a = 3.075$  Å) [47].

The peak feature between 0 and 2 Å in the first coordination shell of  $\text{Ti}_3\text{C}_2\text{T}_x$  is caused by superimposed Ti-O, Ti-F, and Ti-C scattering, where the Ti-C interaction has two different contributions: Ti<sub>I</sub> for the inner Ti atoms that bond only to C, and a second Ti<sub>II</sub> contribution to the outer Ti atoms that bond both to C and to the termination species. The Ti-C bond length of the outer Ti atoms is 0.056 Å longer than that for the inner Ti atoms. Interestingly, the three peaks in the higher coordination shells between 3 and 6 Å also contain a large contribution of *long inclined* single Ti-O and Ti-F scattering paths from all surface Ti atoms to the termination species  $T_x$ , in addition to Ti-Ti scattering and superimposed multiscattering paths, e.g., Ti-Ti-C, Ti-C-O, Ti-C-F, and Ti-F-Ti-F.

The  $\text{Ti-T}_x$  scattering paths exhibit a significant temperature dependence as the data were measured at RT, 250, 550,

and 750 °C. During heating, the peaks become significantly broadened and less intense as observed by the Debye-Waller factor, which increases with the temperature, as a consequence of more atomic vibrations. For the main Ti-Ti scattering,  $\sigma^2$  increases linearly from 0.0066 at room temperature to 0.0082 at 750 °C. A similar trend has been observed in other systems using EXAFS [48]. The broadening is also observed as intensity increases between the peaks in the difference spectra. In addition to the broadening of the peaks, the vibrational behavior and peak broadening exhibit strong anisotropy of the Ti-Ti bonds. Therefore, before each measurement the elevated temperature was stabilized for 20 min and then decreased and stabilized at 250 °C after which the spectra were recorded.

Figure 6 shows the Fourier transform obtained from the  $k^2$ -weighted EXAFS oscillations  $\chi(k)$  of  $\text{Ti}_3\text{C}_2\text{T}_x$  and the effect of the heat treatment, where arrows indicate the general trends. Difference spectra that highlight the temperature-induced changes are shown in the bottom. In the low-radius region of the first coordination shell of the probed Ti (between 1 and 2 Å), including the bonding of the O and F elements, an intensity shift is observed corresponding to an  $\sim 0.2$  Å shorter bond distance. In particular, the F-related intensity decreases indicating desorption of the F upon heating to 750 °C.

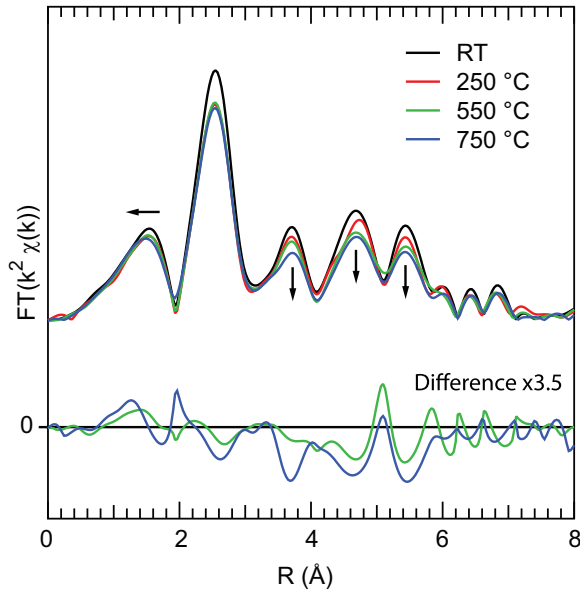


FIG. 6. Temperature-dependent Fourier transforms obtained from Ti 1s EXAFS oscillations  $\chi(k)$  of  $\text{Ti}_3\text{C}_2\text{T}_x$ . Difference spectra ( $\times 3.5$ ) are shown at the bottom.

Contrary to F, the intensity related to O-bonding slightly increases and shifts to shorter bond lengths. This behavior is consistent with previous temperature-dependent core-level XPS results [18] that showed desorption of F and a change of bond site for O in this temperature region.

The three peaks observed between 3 and 6 Å in  $\text{Ti}_3\text{C}_2\text{T}_x$  also occur in EXAFS data of cubic TiC [45,46]. The first peak at  $\sim 3.5$  Å is mainly ascribed to Ti-Ti and Ti-C scattering in the second coordination shell. The second peak at 4.5–5 Å mainly consists of Ti-C-Ti and Ti-Ti-O/F scattering, while the third peak 5.5–6 Å contain many multiscattering paths such as Ti-Ti-Ti (5.30 Å) and Ti-Ti-Ti-C (5.31 Å), etc. However, the intensity of the three peaks in the higher coordination shells also contains a significant contribution of *long inclined* single Ti-O (3.62, 3.73, 4.28, 4.75, 4.79, and 5.04 Å) and Ti-F (3.76, 4.58 Å, 4.78, and 4.86 Å) scattering paths. As observed in the difference spectra, the contributions of these paths decrease as the temperature is increased. This is consistent with the fitting results showing that the Ti-O bond length in the first coordination shell seems to shorten as the temperature increases to 750 °C.

Yet, after a decade of extensive research activities, there is new knowledge to gain about MAX phases and MXenes. In the present study, there are several interesting observations. For example, through XANES we find that the C 2p-Ti 3d hybridization is altered when the  $\text{Ti}_3\text{AlC}_2$  transforms into  $\text{Ti}_3\text{C}_2\text{T}_x$  leading to a smaller crystal-field splitting of the  $t_{2g}$  and  $e_g$  orbitals, which suggests slightly weaker Ti-C bonds in  $\text{Ti}_3\text{C}_2\text{T}_x$  compared to  $\text{Ti}_3\text{AlC}_2$ . Another observation is the 1.4 eV energy shift of the main absorption edge for the  $\text{Ti}_3\text{C}_2\text{T}_x$  compared to  $\text{Ti}_3\text{AlC}_2$ . A main-edge shift is often an indication of a charge redistribution, and when the shift is toward higher energies, the charge transfer is away from the probed atoms. Hence, replacing the weak interacting Al

layers in  $\text{Ti}_3\text{AlC}_2$  with chemisorbed F and O in  $\text{Ti}_3\text{C}_2\text{T}_x$  will withdraw charge from the Ti toward the termination species.

The additional main-edge energy shift caused by the heat treatment, however, cannot be a consequence of a further withdrawal of charge from the Ti atoms, because that would contradict the previous temperature-programmed XPS study [18]; the intensity at the high-binding-energy side of the Ti 2p<sub>3/2</sub> XPS spectra decreases while F desorbs, indicating that Ti in  $\text{Ti}_3\text{C}_2\text{T}_x$  chemically reduces in a heat treatment. In addition, the electronegativity of O is lower compared to F (Pauling scale 3.44 and 3.98, respectively). The Ti 1s XANES main-edge shift toward higher energy must therefore be caused by something else. It can, for example, be a response to the stronger bonding of the O in the fcc site compared to F that pushes the unoccupied Ti 4p orbitals toward higher energy. Regardless of the reason, the Ti 1s XANES shows that orbitals with Ti 4p character are sensitive to changes of the termination species on the fcc sites.

From the EXAFS we learn that the in-plane Ti-Ti distances decrease while the out-of-plane Ti-Ti distances increase when the  $\text{Ti}_3\text{AlC}_2$  is converted into  $\text{Ti}_3\text{C}_2\text{T}_x$ . Concerning EXAFS, it probes the local short-order atomic distances between the absorber atom and the neighboring scatterers using the constructive and destructive interference in the unoccupied electronic structure. Since the EXAFS photoelectrons travel much faster than the speed of the thermal motion of the atoms, the obtained atom distances are an average of “snapshots” that in most cases correspond to the distance between the average atomic positions as obtained with XRD and neutron diffraction, which are considered to be long-order probes. However, if adjacent atoms are moving in an anticorrelated motion, the distance between them will be the same as the atomic positions distance only when both atoms are in-plane, while it will become larger when the atoms are moving in the opposite direction out-of-plane. The atom distances obtained from EXAFS will then be larger than if they would be obtained from XRD and neutron diffraction. The surface Ti atoms and the termination species F and O are expected to move in an anticorrelated motion, and the obtained Ti<sub>II</sub>-O<sub>A</sub>, Ti<sub>II</sub>-O<sub>B</sub>, and Ti<sub>II</sub>-F distances are probably larger than the true atomic positions. This discrepancy between the average atom distances between the  $T_x$  atoms and the surface Ti atoms will become larger with increasing temperature.

#### IV. CONCLUSIONS

Through a combination of XANES and EXAFS we have investigated the MAX phase material  $\text{Ti}_3\text{AlC}_2$  and the MXene material  $\text{Ti}_3\text{C}_2\text{T}_x$ , where the latter was examined before and after a series of heat treatments. The preedge absorption region of both  $\text{Ti}_3\text{AlC}_2$  and  $\text{Ti}_3\text{C}_2\text{T}_x$  shows mainly Ti 1s excitations into two C 2p-Ti 3d hybridized molecular orbitals corresponding to the Ti 3d  $t_{2g}$  and  $e_g$  orbitals. The crystal-field splitting is determined to be 2.9 and 2.2 eV for  $\text{Ti}_3\text{AlC}_2$  and  $\text{Ti}_3\text{C}_2\text{T}_x$ , respectively. The main-edge absorption features originate from the Ti 1s  $\rightarrow$  4p excitation and appear to be sensitive toward the fcc-site occupation, which led to a 1.4 eV



shift when the Al layers in  $\text{Ti}_3\text{AlC}_2$  were replaced with the termination species F and O. The local chemical bonding structure and structural properties with atomic distances in  $\text{Ti}_3\text{C}_2\text{T}_x$  MXene show a significant temperature dependence. Heat treatment up to 750 °C removed F and made the fcc sites available for O occupation, which is manifested as a 0.5 eV high-energy shift of the peaks in the main-edge absorption region.

EXAFS shows that the shortest inplane Ti-Ti atomic distances in  $\text{Ti}_3\text{AlC}_2$  and  $\text{Ti}_3\text{C}_2\text{T}_x$  are 3.032 and 3.016 Å, respectively, which are longer and shorter than the out-of-plane distance of 3.029 Å in  $\text{Ti}_3\text{AlC}_2$  and the corresponding atomic distance in  $\text{Ti}_3\text{C}_2\text{T}_x$  of 3.072 Å. The  $\text{Ti}_I\text{-C}$  and  $\text{Ti}_{II}\text{-C}$  bond lengths in  $\text{Ti}_3\text{AlC}_2$  are 2.220 and 2.160 Å, respectively, while the  $\text{Ti}_I\text{-C}$  and  $\text{Ti}_{II}\text{-C}$  bond lengths in  $\text{Ti}_3\text{C}_2\text{T}_x$  are 2.139 and 2.234 Å, respectively. Significant changes in the Ti-O/F coordination are observed with increasing temperature in the heat treatment. The  $\text{Ti}_{II}\text{-O}$  bond lengths becomes shorter because of a change in coordination from bridge to fcc facilitated through the desorption of the F as the F contribution is found to diminish when the temperature is raised from room temperature up to 750 °C. The significant contribution of *long inclined* single Ti-O and Ti-F scattering paths decreases as the temperature increases.

## ACKNOWLEDGMENTS

We acknowledge MAX IV Laboratory for time on Beamline Balder under Proposals 20190399 and 20191016. Research conducted at MAX IV, a Swedish national user facility, is supported by the Swedish Research Council under contract 2018-07152, the Swedish Governmental Agency for Innovation Systems under contract 2018-04969, and Formas under contract 2019-02496. The computations were enabled by resources provided by the Swedish National Infrastructure for Computing (SNIC) at the National Supercomputer Centre (NSC) partially funded by the Swedish Research Council through Grant Agreement No. 2016-07213. We would also like to thank the Swedish Research Council (VR) LiLi-NFM Linnaeus Environment and Project Grant No. 621-2009-5258. The research leading to these results has received funding from the Swedish Government Strategic Research Area in Materials Science on Functional Materials at Linköping University (Faculty Grant SFO-Mat-LiU No. 2009-00971). M.M. acknowledges financial support from the Swedish Energy Research (Grant No. 43606-1) and the Carl Tryggers Foundation (CTS16:303, CTS14:310). Most importantly, we thank Dr. Joseph Halim at Linköping University for preparing the samples and Kajsa Sigfridsson Clauss at the MAX IV Laboratory for experimental support.

- 
- [1] S. Novoselov, A. K. Geim, S. V. Morozov, D. Jiang, Y. Zhang, S. V. Dubonos, I. V. Grigorieva, and A. A. Firsov, Electric field effect in atomically thin carbon films, *Science* **306**, 666 (2004).
- [2] M. Naguib, M. Kurtoglu, V. Presser, J. Lu, J. Niu, M. Heon, L. Hultman, Y. Gogotsi, and M. W. Barsoum, Two-dimensional nanocrystals produced by exfoliation of  $\text{Ti}_3\text{AlC}_2$ , *Adv. Mater.* **23**, 4248 (2011).
- [3] M. Naguib, O. Mashtalir, J. Carle, V. Presser, J. Lu, L. Hultman, Y. Gogotsi, and M. W. Barsoum, Two-dimensional transition metal carbides, *ACS Nano* **6**, 1322 (2012).
- [4] M. Naguib, V. N. Mochalin, M. W. Barsoum, and Y. Gogotsi, 25th anniversary article: MXenes: A new family of two-dimensional materials, *Adv. Mater.* **26**, 992 (2014).
- [5] Z. Yan, J. Yao, Z. Sun, Y. Zhu, and J. M. Tour, Controlled ambipolar-to-unipolar conversion in graphene field-effect transistors through surface coating with poly(ethylene imine)/poly(ethylene glycol) films, *Small* **8**, 59 (2012).
- [6] Y. Zhou, C. Fuentes-Hernandez, J. Shim, J. Meyer, A. J. Giordano, H. Li, P. Winget, T. Papadopoulos, H. Cheun, and J. Kim, A universal method to produce low-work function electrodes for organic electronics, *Science* **336**, 327 (2012).
- [7] M. Ghidui, M. R. Lukatskaya, M.-Q. Zhao, Y. Gogotsi, and M. W. Barsoum, Conductive two-dimensional titanium carbide ‘clay’ with high volumetric capacitance, *Nature (London)* **516**, 78 (2014).
- [8] M. Naguib, J. Halim, J. Lu, K. M. Cook, L. Hultman, Y. Gogotsi, and M. W. Barsoum, New two-dimensional niobium and vanadium carbides as promising materials for li-ion batteries, *J. Am. Chem. Soc.* **135**, 15966 (2013).
- [9] N. Li, X. Chen, W.-J. Ong, D. R. MacFarlane, X. Zaho, A. K. Cheetham, and C. Sun, Understanding of electrochemical mechanisms for  $\text{CO}_2$  capture and conversion into hydrocarbon fuels in transition-metal carbides (MXenes), *ACS Nano* **11**, 10825 (2017).
- [10] J. Halim, M. R. Lukatskaya, K. M. Cook, J. Lu, C. R. Smith, L.-Å. Näslund, S. J. May, L. Hultman, Y. Gogotsi, P. Eklund, and M. W. Barsoum, Transparent conductive two-dimensional titanium carbide epitaxial thin films, *Chem. Mater.* **26**, 2374 (2014).
- [11] X. Li, X. Yin, C. Song, M. Han, H. Xu, W. Duan, L. Cheng, and L. Zhang, Self-assembly core-shell graphene-bridged hollow MXenes spheres 3D foam with ultrahigh specific EM absorption performance, *Adv. Funct. Mater.* **28**, 1803938 (2018).
- [12] M. W. Barsoum, *MAX Phases: Properties of Machinable Ternary Carbides and Nitrides* (Wiley, New York, 2013).
- [13] M. Sokol, V. Natsu, S. Kota, and M. W. Barsoum, On the chemical diversity of the MAX phases, *Trends Chem.* **1**, 210 (2019).
- [14] M. Khazaei, M. Arai, T. Sasaki, C.-Y. Chung, N. S. Venkataramanan, M. Estili, Y. Sakka, and Y. Kawazoe, Novel electronic and magnetic properties of two-dimensional transition metal carbides and nitrides, *Adv. Funct. Mater.* **23**, 2185 (2013).
- [15] Y. Xie and P. R. C. Kent, Hybrid density functional study of structural and electronic properties of functionalized  $\text{Ti}_{n+1}\text{X}_n$  ( $X = \text{C}, \text{N}$ ) monolayers, *Phys. Rev. B* **87**, 235441 (2013).
- [16] Q. Tang, Z. Zhou, and P. Shen, Are MXenes promising anode materials for Li ion batteries? Computational studies on electronic properties and Li storage capability of  $\text{Ti}_3\text{C}_2$  and  $\text{Ti}_3\text{C}_2\text{X}_2$  ( $X = \text{F}, \text{OH}$ ) monolayer, *J. Am. Chem. Soc.* **134**, 16909 (2012).
- [17] Z. H. Fu, Q. F. Zhang, D. Legut, C. Si, T. C. Germann, T. Lookman, S. Y. Du, J. S. Francisco, and R. F. Zhang, Stabilization and strengthening effects of functional groups in two-dimensional titanium carbide, *Phys. Rev. B* **94**, 104103 (2016).

- [18] I. Persson, L.-Å. Näslund, J. Halim, M. W. Barsoum, V. Darakchieva, J. Palisaitis, J. Rosen, and P. O. Å. Persson, On the organization and thermal behavior of surface functional groups on  $\text{Ti}_3\text{C}_2$  MXene in vacuum, *2D Mater.* **5**, 015002 (2017).
- [19] T. Hu, M. Hu, B. Gao, W. Li, and X. Wang, Screening surface structure of MXenes by high-throughput computation and vibrational spectroscopic confirmation, *J. Phys. Chem. C* **122**, 18501 (2018).
- [20] P. O. Å. Persson, and J. Rosen, Current state of the art on tailoring the MXene composition, structure, and surface chemistry, *Curr. Opin. Solid State Mater. Sci.* **23**, 100774 (2019).
- [21] R. A. Bair and W. A. Goddard III, *Ab initio* studies of the x-ray absorption edge in copper complexes. I. Atomic  $\text{Cu}^{2+}$  and  $\text{Cu}(\text{II})\text{Cl}_2$ , *Phys. Rev. B* **22**, 2767 (1980).
- [22] J. Kawai, Absorption techniques in x-ray spectroscopy, in *Encyclopedia of Analytical Chemistry*, edited by R. A. Meyers (Wiley, Chichester, 2000), p. 13288.
- [23] V. S. R. Bordwehr, A history of x-ray absorption fine structure, *Am. Phys. Fr.* **14**, 377 (1989).
- [24] M. R. Lukatskaya, S.-M. Bak, X. Yu, X.-Q. Yang, M. W. Barsoum, and Y. Gogotsi, Probing the mechanism of high capacitance in 2D titanium carbide using in situ x-ray absorption spectroscopy, *Adv. Energy Mater.* **5**, 1500589 (2015).
- [25] Z. Li, L. Yu, C. Milligan, T. Ma, L. Zhou, Y. Cui, Z. Qi, N. Libretto, B. Xu, J. Luo, E. Shi, Z. Wu, H. Xin, W. N. Delgass, J. T. Miller, and Y. Wu, Two-dimensional transition metal carbides as supports for tuning the chemistry of catalytic nanoparticles, *Nat. Commun.* **9**, 5258 (2018).
- [26] D. Zhao, Z. Chen, W. Yang, S. Liu, X. Zhang, Y. Yu, W.-C. Cheong, L. Zheng, F. Ren, G. Ying, X. Cao, D. Wang, Q. Peng, G. Wang, and C. Chen, MXene ( $\text{Ti}_3\text{C}_2$ ) vacancy-confined single-atom catalyst for efficient functionalization of  $\text{CO}_2$ , *J. Am. Chem. Soc.* **141**, 4086 (2019).
- [27] E. Piskorska, K. Lawniczka-Jablonska, I.N. Demchenko, R. Minikayev, E. Benko, P. Klimczyk, A. Witkowska, E. Welter, and M. Heinonen, Characterization of the c-BN/TiC,  $\text{Ti}_3\text{SiC}_2$  systems by element selective spectroscopy, *J. Alloys Compd.* **382**, 187 (2004).
- [28] E. Benko, P. Klimczyk, S. Mackiewicz, T. L. Barr, and E. Piskorska, cBN-TiSiC composites, *Diam. Relat. Mater.* **13**, 521 (2004).
- [29] Z. Li, Y. Cui, Z. Wu, C. Milligan, L. Zhou, G. Mitchell, B. Xu, E. Shi, J. T. Miller, F. H. Ribeiro, and Y. Wu, Reactive metal-support interactions at moderate temperature in two-dimensional niobium-carbide supported platinum catalysts, *Nat. Catal.* **1**, 349 (2018).
- [30] E. B. Deeva, A. Kurlov, P. M. Abdala, D. Lebedev, S. M. Kim, C. P. Gordon, A. Tsoukalou, A. Fedorov, and C. R. Müller, In situ XANES/XRD study of the structural stability of two-dimensional molybdenum carbide  $\text{Mo}_2\text{CT}_x$ : Implications for the catalytic activity in the water-gas shift reaction, *Chem. Mater.* **31**, 4505 (2019).
- [31] M. Magnuson, J. Halim, and L.-Å. Näslund, Chemical bonding in carbide MXene nanosheets, *J. Electron. Spectrosc.* **224**, 27 (2018).
- [32] J. J. Rehr, J. J. Kas, F. D. Vila, M. P. Prange, and K. Jorissen, Parameter-free calculations of x-ray spectra with FEFF9, *Phys. Chem. Chem. Phys.* **12**, 5503 (2010).
- [33] J. J. Rehr, J. J. Kas, M. P. Prange, A. P. Sorini, Y. Takimoto, and F. D. Vila, *Ab initio* theory and calculations of x-ray spectra, *C. R. Phys.* **10**, 548 (2009).
- [34] J. J. Rehr and R. C. Albers, Theoretical approaches to x-ray absorption fine structure, *Rev. Mod. Phys.* **72**, 621 (2000).
- [35] K. V. Klementev, Extraction of the fine structure from x-ray absorption spectra, *J. Phys. D* **34**, 209 (2001).
- [36] E. A. Stern, Theory of the extended x-ray-absorption fine structure, *Phys. Rev. B* **10**, 3027 (1974).
- [37] E. A. Stern, Structural determination by x-ray Absorption, *Contemp. Phys.* **19**, 289 (1978).
- [38] E. A. Stern and S. M. Heald, *Basic Principles and Applications of EXAFS; Handbook of Synchrotron Radiation* (North-Holland, New York, 1983).
- [39] T. Yamamoto, Assignment of pre-edge peaks in K-edge x-ray absorption spectra of 3d transition metal compounds: electric dipole or quadrupole? *x-Ray Spectrom.* **37**, 572 (2008).
- [40] N. Jiang, D. Su, and J. C. H. Spence, Determination of Ti coordination from pre-edge peaks in Ti K-edge XANES, *Phys. Rev. B* **76**, 214117 (2007).
- [41] F. Farges, G. E. Brown, and J. J. Rehr, Ti K-edge XANES studies of Ti coordination and disorder in oxide compounds: Comparison between theory and experiment, *Phys. Rev. B* **56**, 1809 (1997).
- [42] D. Cabaret, A. Bordage, A. Juhin, M. Arfaouia, and E. Gaudryad, First-principles calculations of x-ray absorption spectra at the K-edge of 3d transition metals: an electronic structure analysis of the pre-edge, *Phys. Chem. Chem. Phys.* **12**, 5619 (2010).
- [43] C. A. Triana, C. M. Araujo, R. Ahuja, G. A. Niklasson, and T. Edvinsson, Electronic transitions induced by short-range structural order in amorphous  $\text{TiO}_2$ , *Phys. Rev. B* **94**, 165129 (2016).
- [44] T. C. Rossi, D. Grolimund, M. Nachtegaal, O. Cannelli, G. F. Mancini, C. Bacellar, D. Kinschel, J. R. Rouxel, N. Ohannessian, D. Pergolesi, T. Lippert, and M. Chergui, x-ray absorption linear dichroism at the Ti K edge of anatase  $\text{TiO}_2$  single crystals, *Phys. Rev. B* **100**, 245207 (2019).
- [45] A. Balzarotti, M. De Crescenzi, and L. Incoccia, Electronic relaxation effects on x-ray spectra of titanium and transition-metal carbides and nitrides, *Phys. Rev. B* **25**, 6349 (1982).
- [46] C. Adelhelm, M. Balden, and M. Sikora, EXAFS investigation of the thermally induced structuring of titanium-doped amorphous carbon films, *Mater. Sci. Eng. C* **27**, 1423 (2007).
- [47] JCPDS-International Centre for Diffraction Data, Titanium metal (Ti): Ref. ID 00-044-1294.
- [48] W. S. Chu, S. Zhang, M. J. Yu, L. R. Zheng, T. D. Hu, H. F. Zhao, A. Marcelli, A. Bianconi, N. L. Saini, W. H. Liu, and Z. Y. Wu, Correlation between local vibrations and metal mass in  $\text{AlB}_2$ -type transition-metal diborides, *J. Synch. Rad.* **16**, 30 (2009).